Elucidating the Methylammonium (MA) Conformation in MAPbBr$_3$ Perovskite with Application in Solar Cells

Carlos A. López,[†,§] María Victoria Martínez-Huerta,[‡] María Consuelo Alvarez-Galván,[‡] Paula Kayser,[†] Patricia Gant,[∥] Andres Castellanos-Gomez,[†][iD] María T. Fernández-Díaz,[⊥] Francois Fauth,[#] and José A. Alonso*,[†][iD]

[†]Instituto de Ciencia de Materiales de Madrid and [‡]Instituto de catálisis y Petroleoquímica, CSIC, Cantoblanco 28049, Spain

[§]INTEQUI, Universidad Nacional de San Luis, CONICET, Facultad de Química, Bioquímica y Farmacia, Chacabuco y Pedernera, 5700 San Luis, Argentina

[∥]Instituto Madrileño de Estudios Avanzados en Nanociencia (IMDEA Nanociencia), Campus de Cantoblanco E-28049, Spain

[⊥]Institut Laue Langevin, BP 156X, Grenoble F-38042, France

[#]CELLS−ALBA synchrotron, E-08290 Cerdanyola del Valles, Spain

S *Supporting Information*

ABSTRACT: Hybrid organic−inorganic perovskites, MAPbX$_3$ (X = halogen), containing methylammonium (MA: CH$_3$−NH$_3^+$) in the large voids conformed by the PbX$_6$ octahedral network, are the active absorption materials in the new generation of solar cells. CH$_3$NH$_3$PbBr$_3$ is a promising member with a large band gap that gives rise to a high open circuit voltage. A deep knowledge of the crystal structure and, in particular, the MA conformation inside the perovskite cage across the phase transitions undergone below room temperature, seems essential to establish structure−property correlations that may drive to further improvements. The presence of protons requires the use of neutrons, combined with synchrotron XRD data that help to depict subtle symmetry changes undergone upon cooling. We present a consistent picture of the structural features of this fascinating material, in complement with photocurrent measurements from a photodetector device, demonstrating the potential of MAPbBr$_3$ in optoelectronics.
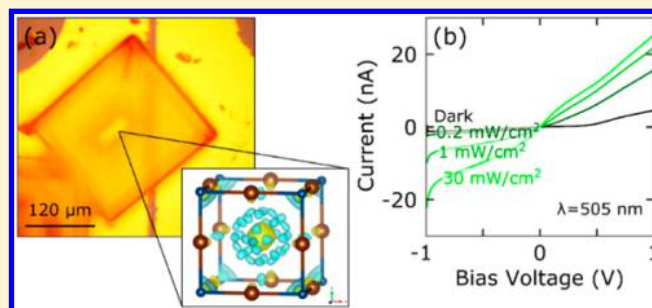
1. INTRODUCTION

Organic−inorganic hybrid perovskites have emerged as promising materials for the next generation of solar cells because of their ease of fabrication and performances rivaling the best thin-film photovoltaic devices.[1−5] The introduction of CH$_3$NH$_3$PbX$_3$ (X = Br and I) by Miyasaka et al. as a sensitizer in an electrolyte-based solar cell structure marked the beginning of perovskite-based photovoltaics.[2] However, the power conversion efficiency (PCE) and cell stability were poor due to the corrosion of the perovskites by the liquid electrolyte. A key advance was made in 2012 by replacing the liquid electrolyte with a solid hole-transporting material, which resulted in both high PCE of 9.7% and enhanced cell stability.[3] Since then, an intensive research has been devoted to the improvement of halide perovskite-based solar cells, where a variety of cell architectures have been developed increasing the PCEs to 22.1% over the past years.[6]

Fundamental studies have revealed the superior optical and electrical properties of halide perovskites, including the tunability of the band gap by varying the halide (i.e., bromide, iodide) composition of the perovskite precursor solution,[7−9] the high absorption coefficient,[10] and the long lifetime of photogenerated species.[11] CH$_3$NH$_3$PbI$_3$-based perovskite solar cells have been a primary focus due to their near-complete visible light absorption in films <1 μm and their fast charge extraction rates.[11,12] However, the poor stability of CH$_3$NH$_3$PbI$_3$ and rapid degradation in humidity has remained a major obstacle for commercialization.[13,14] CH$_3$NH$_3$PbBr$_3$ is a promising alternative to CH$_3$NH$_3$PbI$_3$ with a large band gap of 2.2 eV, which gives rise to a high open-circuit voltage ($V_{oc} \approx$ 1.2−1.5 V).[15,16] Their long exciton diffusion length (>1.2 μm) enables good charge transport in devices.[17] In addition, CH$_3$NH$_3$PbBr$_3$ demonstrates higher stability toward air and moisture due to its stable cubic phase and low ionic mobility relative to the pseudocubic CH$_3$NH$_3$PbI$_3$, in which inherent lattice strain provides an avenue for increased diffusion.[7,17−19] These features may compensate for a relatively large exciton binding energy (76 meV) and reduced light absorption beyond its band edge at 550 nm, accounting for a more limited efficiencies of CH$_3$NH$_3$PbBr$_3$ solar cells.[7,18,20−22]

In parallel with the evaluation of the performance contributed by a particular chemical substitution, it is necessary to undertake a suitable crystallographic characterization in the same state or under conditions in which the sample will be used. It is of paramount importance to unveil the details of the crystal structure in relation to the physical behavior, such as $CH_3–NH_3^+$ (methylammonium, MA) delocalization, anisotropic displacement factors, tilting of polyhedra, and so on. This knowledge is essential to establish relationships between the structures and the macroscopic phenomenology. MAPbBr$_3$ was previously studied by diffraction techniques in single crystal form by X-ray or in deuterated sample by neutron beams.[23−25] In this work, we study the crystallographic features in a powdered, nondeuterated sample from neutron and synchrotron X-ray diffraction at different temperatures. From these techniques, we describe the evolution of the orientation of MA group in the 120−295 K temperature range.

2. EXPERIMENTAL SECTION

MAPbBr$_3$ (MA: methylammonium) was crystallized as an orange microcrystalline powder from a solution of stoichiometric amounts of PbBr$_2$ and MABr in dimethylformamide. The crystals were ground prior to the diffraction experiments. Laboratory XRPD patterns were collected on a Bruker D5 diffractometer with Cu Kα (λ = 1.5418 Å) radiation; the 2θ range was 4−90° with increments of 0.03°. The thermal evolution of the crystallographic structure was studied by synchrotron X-ray powder diffraction (SXRPD) at 120, 150, 180, 210, 240, and 270 K and room temperature (RT, 298 K). SXRPD patterns were collected in high angular resolution mode (so-called MAD setup) on the MSPD diffractometer in ALBA synchrotron at Barcelona, Spain, selecting an incident beam with 38 keV energy, λ= 0.3252 Å.[26] The sample was contained in a 0.3 mm diameter quartz capillary that was rotating during the data acquisition. Additionally, a NPD pattern at RT was collected on the D2B diffractometer, Laue Langevin Institut (ILL), Grenoble, France, with a wavelength of 1.594 Å in the high-flux mode. The nondeuterated sample was contained in a 6 mm diameter vanadium cylinder; the counting time was 2 h. The coherent scattering lengths for Pb, Br, C, N and H were, 9.405, 6.795, 6.646, 9.36, and −3.739 fm, respectively. XRPD, SXRPD, and NPD diffraction patterns were analyzed with the Rietveld method using the FullProf program.[27,28] A photodetector device was fabricated by drop-casting the perovskite solution in dimethylformamide onto Au/Cr prepatterned electrodes with a gap of 10 μm, and drying in a hot plate at 100 °C.

3. RESULTS AND DISCUSSION

3.1. Synchrotron X-ray Powder Diffraction. Laboratory XRPD patterns at RT are similar to those previously reported for this phase;[23] no impurities were observed (Figure S1). The crystal structure was reported at RT as cubic in the space group $Pm\overline{3}m$ using X-ray single crystal diffraction.[23] Attempts to fit the pattern to this symmetry were not satisfactory, since the sample exhibits strong preferred orientation that cannot be simulated. However, a Le Bail fit to the cubic symmetry was successful (Figure S1), obtaining a cell parameter a = 5.9595(1) Å.

Even though the crystal structure was successfully analyzed from the SXRPD patterns, using high-energy synchrotron X-rays in transmission mode contributed to a better powder averaging from rotating capillaries, hence minimizing the preferred orientation. The thermal evolution of the crystallographic structure was followed between 120 K and RT. In this temperature range, two phase transitions were observed, as previously reported by Swaison et al.[23] The patterns collected at RT, 270, and 240 K were refined as cubic in $Pm\overline{3}m$ space

group, at 210 and 180 K as tetragonal in $I4/mcm$ space group, and at 120 K as orthorhombic in $Pnma$ space group. At 150 K, transient diffraction lines were observed, which could not be indexed either as tetragonal or as orthorhombic. Figure 1 shows the thermal evolution of selected diffraction lines.
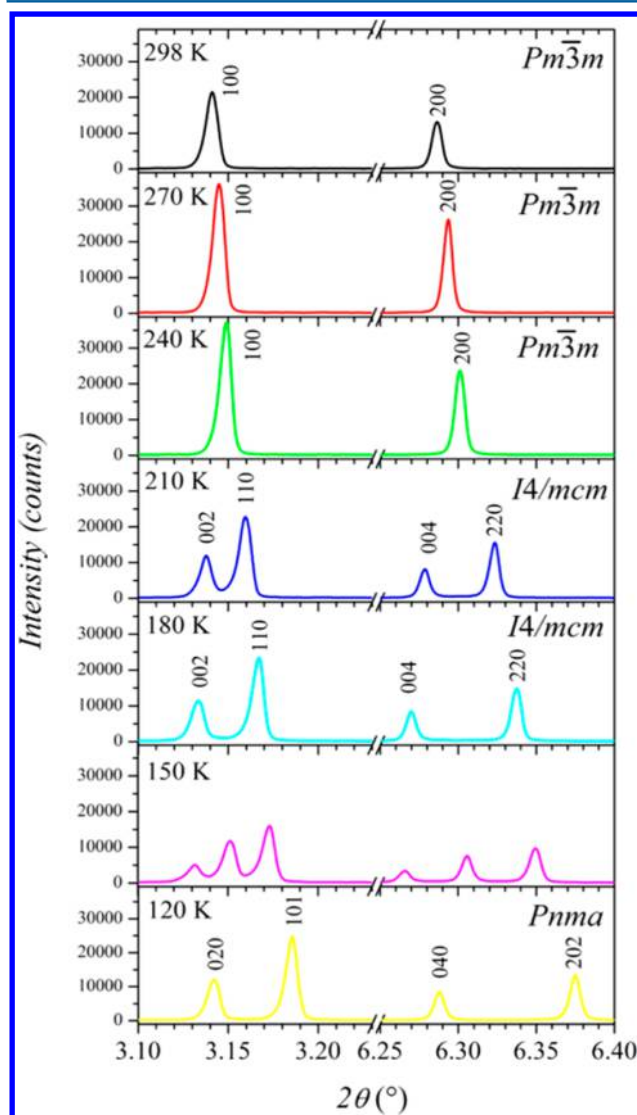

Figure 1. Thermal evolution of selected diffraction lines in which the phase transitions are evidenced, from SXRPD data.

In the high-temperature model ($Pm\overline{3}m$), the lead and bromine atoms were placed in 1a (0,0,0) and 3d (1/2,0,0) positions, respectively. Then, a difference Fourier synthesis map was obtained from the observed and calculated powder diffraction data. Figure 2a shows the electron density as a contour surface at 2.2 e for the pattern collected at RT, corresponding to C and N atoms of the MA unit. The observed positive density suggests that C/N atoms are located at large multiplicity 24i (0.5, y, y) sites. This fact unveils that MA is delocalized between six different positions all aligned along [110] direction. After adding the C/N atoms to the structural model, the structure can be correctly refined at RT. The Rietveld plot is included in Figure S2. When the same procedure is carried out at 270 and 240 K, several differences in the electron density were observed. Figure 2b illustrates these differences in the zone where the MA unit is located. At 270 K,
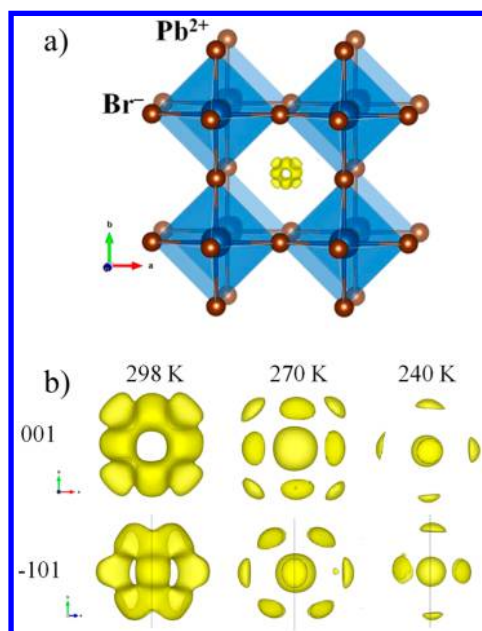
Figure 2. (a) Schematic view of lead (blue spheres) and bromine (brown spheres) atoms in the cubic system. The isosurface of electron density at 2.2 e is shown in yellow. (b) Thermal evolution of electron density (in the three cases at 2.2 e) along 001 and −101 directions.

Figure 3. Schematic view of MAPbBr$_3$ at 210 K in the tetragonal system along [1$\bar{1}$0]. The isosurface of electron density at 3.2 e is shown in yellow. The visualized atoms are limited in order to keep a view related to to the cubic system.

Figure 4. Schematic view of MAPbBr$_3$ at 120 K in the orthorhombic system. The visualized C and N atoms from MA are oriented within (101) plane. At this temperature, the MA units are no longer delocalized.

the delocalization of MA is similar to that at RT (along [110] directions), but a clear decrease in the thermal vibrations is revealed. However, a drastic change in the delocalization is observed at 240 K: Figure 2b shows that the MA units are aligned along [100] directions, reducing their delocalization as temperature decreases. The best structural fits, taking into account the MA delocalization, are displayed in Figure S2, and the corresponding crystallographic data are listed in Tables S1–S3, for RT, 270, and 240 K, respectively.

The patterns collected at 210 and 180 K show a clear tetragonal distortion, see Figure 1, and the structure was refined (I4/mcm space group) locating Pb at 4c (0, 0, 0) and Br at 4a (0, 0, 1/4) and 8h (x, x + 1/2, 0) positions. At this point, the difference Fourier synthesis maps at both temperatures unveiling the missing electron density indicate that the MA units are delocalized as in the cubic system (see Figure 3). Two different densities are determined, corresponding to 16l Wyckoff site. Therefore, C and N atoms were located at this position and fitted with a distance constraint of 1.49 Å (standard deviation of 0.04 Å) in order to keep up the chemical restraints of MA. The structures at 210 and 180 K were correctly refined; the Rietveld plots are displayed in Figure S3. The crystallographic parameters at 210 and 180 K are listed in Tables S4 and S5, respectively.

At 150 K, some transient diffraction lines were observed, which could not be indexed either as tetragonal or as orthorhombic and must belong to an intermediate structure with a narrow stability range. The presence of a hypothetical Imma phase, observed in a number of simple perovskites (for example, SrRuO$_3$)[29] was discarded from our synchrotron data at 150 K.

At the lowest measured temperature, 120 K, the pattern was successfully refined in the orthorhombic symmetry (Pnma). Figure 4 shows the final structure obtained in the Pnma space group at 120 K, where all parameters were refined (positions and anisotropic ADPs). The pancake shape of the bromine
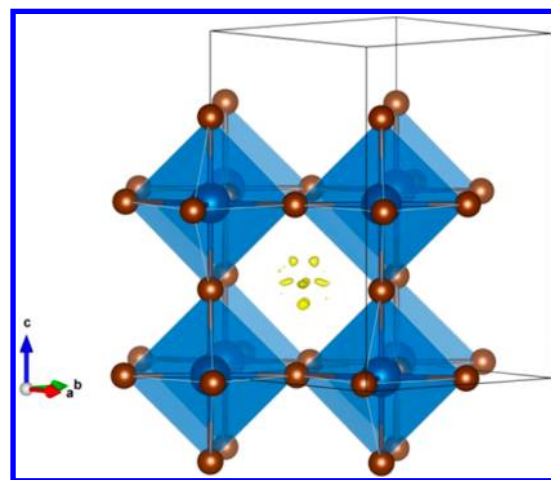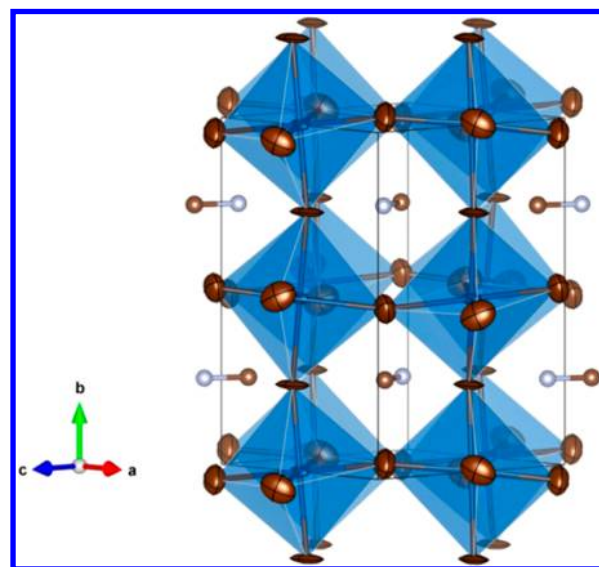
ADPs as an oblate spheroid locks the bromine atoms at mid-lead positions with enhanced vibrations perpendicular to the Pb−Pb distance, as frequently observed in many perovskite compounds.[30]

The good agreement between observed and calculated profiles is shown in Figure S4, whereas the crystallographic parameters are listed in Table S6. As depicted in Figure 4, in this model the MA groups are not delocalized but oriented and contained in the (010) plane. Figures S5 and S6 additionally illustrate the structural evolution below RT.

3.2. Neutron Powder Diffraction. To complement the SXRPD study, yielding information on the C and N positions of the MA units, a neutron diffraction investigation was essential to locate H atoms and elucidate the MA conformation in the lattice. Up to now, only three works are devoted to describe the methylammonium position (including the H atoms) in this perovskite. Two of them use single-crystal

neutron diffraction,[24,25] and the third one uses the powder method, but with a deuterated sample.[23] In the present study, a NPD pattern was collected in a nondeuterated sample. Unquestionably, the fact that the incoherent scattering from hydrogen atoms generates a large background, together with a low Q contribution from the inelastic scattering of methyl groups might be inconvenient. For this reason, the background was modeled from a list of intensity versus 2 theta values selected manually from the experimental data in angular regions devoid of reflections. In the final run, these intensities were also refined to optimize the background level. Thus, the quality of the Rietveld refinement is not affected by the high background level. A correct statistic is reached for the crystallographic peaks given the high neutron flux at the sample.

At RT, the initial model for the cubic structure concerned only the lead and bromine atoms, placed at $1a$ $(0, 0, 0)$ and $3d$ $(1/2, 0, 0)$ positions. This model gave a very poor fit to the neutron data, since the contribution of the H, C, and N atoms is very important. At this point, a difference Fourier synthesis from the observed and calculated NPD data yielded the positive (yellow) and negative (blue) isosurfaces shown in Figure 5,
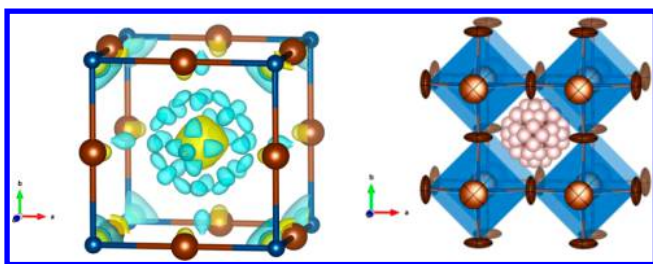

Figure 5. (left) Schematic view of nuclear density (scattering length density) of MAPbBr$_3$ at room temperature. The negative and positive isosurfaces are at 0.12 and 0.25 fm, respectively. (right) Crystal structure obtained from NPD refinement.

which correspond to the H and C/N positions, respectively. These nuclear densities support that the MA units are delocalized in the A site of the perovskite. Considering the positive density, the C/N atoms are located at $24i$ $(0.5, y, y)$ positions, as previously determined from SXRPD data. Then, the H positions can be elucidated from the geometric shape of methylammonium group. The observed geometry can be satisfied with two hydrogen atoms located at $24l$ $(0.5, y, z)$ and $48n$ (x, y, z) Wyckoff sites. The Rietveld refinement of the positions of C/N and H atoms provides an excellent agreement between observed and calculated NPD data at RT; moreover, a marked improvement is obtained after the refinement of the displacement factors. Pb, Br, and C/N atoms were refined with anisotropic displacement parameters while the H atoms with isotropic factors. This improvement is mainly observed in the R_{Bragg} factor, which decreases from 12.7 to 3.9% when the anisotropic displacement factors are considered.

The good fit between observed and calculated neutron data is shown in Figure 6. The atomic parameters are listed in Table S7.

The obtained results agree with those previously informed by Mashiyama et al.[24] but subtly differ from that reported by Baikie et al.[25] The difference resides in the C/N positions. In the present work these atoms are located in $24i$ $(0.5, y, y)$ site, while in the Baikie et al. work, they were located in $24l$ $(0.5, y, z)$ site. This was elucidated from Fourier difference maps where the density is perfectly aligned along the interaxial direction for
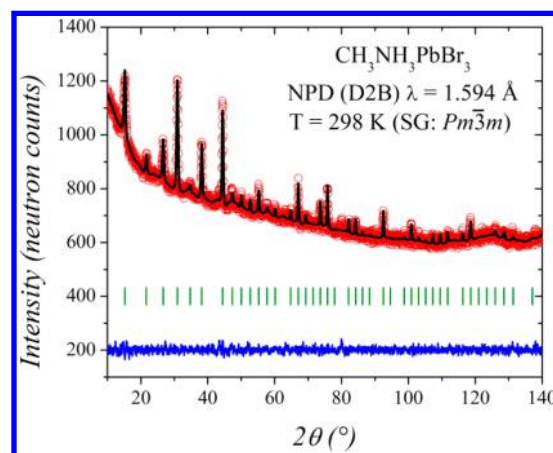

Figure 6. Observed (red circles), calculated (black line), and difference (blue line) neutron diffraction pattern at room temperature in the cubic system, space group $Pm\bar{3}m$..

both neutron powder diffraction (NPD) and SXRPD data; see Figure 2b along $[\bar{1}01]$ direction. Then, the model of Baikie et. al was also tested, and refined y and z values for C/N atoms at $24l$ sites are indistinguishable within experimental error. The difference between models may seem insignificant, but is very important to establish the orientations of methylammonium group in the lattice. The possible orientations were already studied and classified in models A, B, or C where the MA are oriented along $[100]$, $[110]$, and $[111]$ directions, respectively.[31] As can be seen, the preferred orientation in our case corresponds to the model B. In this case the MA distribution in the cubic phase can be deconvoluted in different directions at room temperature or at 240 K. Figure 7 represents the possible
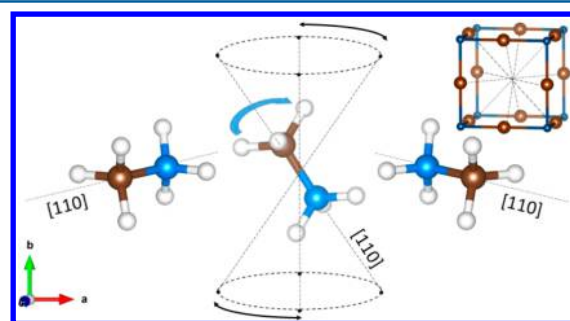

Figure 7. Schematic view of MA distribution in the cubic phase at room temperature.

orientations in which MA resonates along $[110]$ direction at room temperature. In contrast, at 240 K the MA orientations are more restricted and respond to model A.[31] Figures S7 and S8 illustrate the different directions along which the MA can be found at RT and at 240 K, respectively.

3.3. Electro-Optic Characterization. In order to illustrate the potential of the synthesized CH$_3$NH$_3$PbBr$_3$ in optoelectronic applications, we designed a photodetector device (Figure 8a) fabricated by drop-casting the perovskite solution onto Au/Cr prepatterned electrodes. Figure 8b shows the current–voltage (I–V) characteristics of the device under illumination at 505 nm for different incident optical power densities. The photoresponse exhibited by this device is among the largest ones reported for other perovskite-based photodetectors with different geometries: 2D-MAPbI$_3$,[32,33] thin films[34,35] nano-
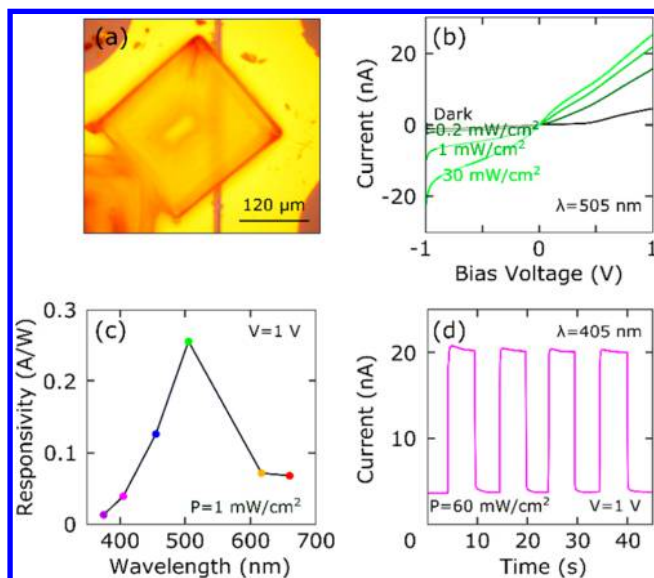
Figure 8. (a) Optical image of a photodetector device with a crystal grown between two prepatterned electrodes. (b) Current–voltage (I–V) curves under illumination at 505 nm for different incident optical power densities. (c) Responsivity spectrum for different wavelengths. (d) Photo current through the device as a function of time with a fixed voltage under modulated illumination.

wires[36,37] and networks.[38] We performed I–V measurements by employing light sources with different wavelengths all at the same illumination power of 1 mW/cm^2.

We extract the wavelength responsivity spectrum of the photodetector (shown in Figure 8c), by using the following formula:

$$R = \frac{I_{ph}}{P}$$

with R the responsivity, I_{ph} the generated photocurrent, and P the illumination power on the device. We observe a maximum in the responsivity (0.26 A/W) for light with wavelength of 505 nm, which is near to the wavelength with maximum solar irradiance. Finally, in Figure 8d we plot the current through the device as a function of time with a fixed voltage under pulsed illumination. This illumination mode allows us to characterize the response time of the photodetector, in this device <100 ms (limited by the experimental setup). The limit of the response time obtained is comparable with values previously reported.[32,33,39,40]

4. CONCLUSIONS

We show that MAPbBr$_3$ is a promising photodetector material with an excellent responsivity for the more intense radiation of the solar spectrum, around 500 nm. We have deepened into the knowledge of the crystal structure and answered questions regarding the MA conformation inside the perovskite cage, which conspicuously evolve across the phase transitions that this material experiences below room temperature. A partial delocalization in the RT cubic phase, where C and N atoms adopt large multiplicity positions, evolve to a localization in the orthorhombic structure at 120 K, where MA units are oriented within (101) plane. A profound knowledge of the crystal structure details seems essential to establish structure–property correlations that may drive to further improvements.

■ ASSOCIATED CONTENT

Ⓢ Supporting Information

The Supporting Information is available free of charge on the ACS Publications website at DOI: 10.1021/acs.inorg-chem.7b02344.

Listings of Rietveld refinement plots, crystal structures, and tables with crystallographic data (PDF)

■ AUTHOR INFORMATION

Corresponding Author

*E-mail: ja.alonso@icmm.csic.es.

ORCID Ⓘ

Andres Castellanos-Gomez: 0000-0002-3384-3405

José A. Alonso: 0000-0001-5329-1225

Notes

The authors declare no competing financial interest.

■ REFERENCES

(1) Lee, M. M.; Teuscher, J.; Miyasaka, T.; Murakami, T. N.; Snaith, H. J. Efficient hybrid solar cells based on meso-superstructured organometal halide perovskites. *Science* **2012**, *338*, 643–647.

(2) Kojima, A.; Teshima, K.; Shirai, Y.; Miyasaka, T. Organometal Halide Perovskites as Visible-Light Sensitizers for Photovoltaic Cells. *J. Am. Chem. Soc.* **2009**, *131*, 6050–6051.

(3) Kim, H.-S.; Lee, C.-R.; Im, J.-H.; Lee, K.-B.; Moehl, T.; Marchioro, A.; Moon, S.-J.; Humphry-Baker, R.; Yum, J.-H.; Moser, J. E.; Grätzel, M.; Park, N.-G. Lead Iodide Perovskite Sensitized All-Solid-State Submicron Thin Film Mesoscopic Solar Cell with Efficiency Exceeding 9%. *Sci. Rep.* **2012**, *2*, 591.

(4) Ye, M.; Hong, X.; Zhang, F.; Liu, X. Recent advancements in perovskite solar cells: flexibility, stability and large scale. *J. Mater. Chem. A* **2016**, *4*, 6755–6771.

(5) Fan, Z.; Sun, K.; Wang, J. Perovskites for photovoltaics: a combined review of organic–inorganic halide perovskites and ferroelectric oxide perovskites. *J. Mater. Chem. A* **2015**, *3*, 18809–18828.

(6) Green, M. A.; Emery, K.; Hishikawa, Y.; Warta, W.; Dunlop, E. D. *Prog. Photovoltaics* **2016**, *24*, 905–913.

(7) Noh, J. H.; Im, S. H.; Heo, J. H.; Mandal, T. N.; Seok, S. I. Chemical Management for Colorful, Efficient, and Stable Inorganic–Organic Hybrid Nanostructured Solar Cells. *Nano Lett.* **2013**, *13*, 1764–1769.

(8) Sadhanala, A.; Deschler, F.; Thomas, T. H.; Dutton, S. E.; Goedel, K. C.; Hanusch, F. C.; Lai, M. L.; Steiner, U.; Bein, T.; Docampo, P.; Cahen, D.; Friend, R. H. Preparation of Single-Phase Films of CH$_3$NH$_3$Pb(I$_{1-x}$Br$_x$)$_3$ with Sharp Optical Band Edges. *J. Phys. Chem. Lett.* **2014**, *5*, 2501–2505.

(9) Eperon, G. E.; Stranks, S. D.; Menelaou, C.; Johnston, M. B.; Herz, L. M.; Snaith, H. J. Formamidinium lead trihalide: a broadly tunable perovskite for efficient planar heterojunction solar cells. *Energy Environ. Sci.* **2014**, *7*, 982–988.

(10) De Wolf, S.; Holovsky, J.; Moon, S.-J.; Löper, P.; Niesen, B.; Ledinsky, M.; Haug, F.-J.; Yum, J.-H.; Ballif, C. Organometallic Halide

Perovskites: Sharp Optical Absorption Edge and Its Relation to Photovoltaic Performance. *J. Phys. Chem. Lett.* **2014**, *5*, 1035−1039.

(11) Stranks, S. D.; Eperon, G. E.; Grancini, G.; Menelaou, C.; Alcocer, M. J. P.; Leijtens, T.; Herz, L. M.; Petrozza, A.; Snaith, H. J. Electron-Hole Diffusion Lengths Exceeding 1 Micrometer in an Organometal Trihalide Perovskite Absorber. *Science* **2013**, *342*, 341−344.

(12) Xing, G.; Mathews, N.; Sun, S.; Lim, S. S.; Lam, Y. M.; Grätzel, M.; Mhaisalkar, S.; Sum, T. C. Long-range balanced electron- and hole-transport lengths in organic-inorganic $CH_3NH_3PbI_3$. *Science* **2013**, *342*, 344−347.

(13) Han, Y.; Meyer, S.; Dkhissi, Y.; Weber, K.; Pringle, J. M.; Bach, U.; Spiccia, L.; Cheng, Y.-B. Degradation observations of encapsulated planar $CH_3NH_3PbI_3$ perovskite solar cells at high temperatures and humidity. *J. Mater. Chem. A* **2015**, *3*, 8139−8147.

(14) Yang, J.; Siempelkamp, B. D.; Liu, D.; Kelly, T. L. Investigation of $CH_3NH_3PbI_3$ Degradation Rates and Mechanisms in Controlled Humidity Environments Using in Situ Techniques. *ACS Nano* **2015**, *9*, 1955−1963.

(15) Zheng, X.; Chen, B.; Wu, C.; Priya, S. Room temperature fabrication of $CH_3NH_3PbBr_3$ by anti-solvent assisted crystallization approach for perovskite solar cells with fast response and small J−V hysteresis. *Nano Energy* **2015**, *17*, 269−278.

(16) Arora, N.; Orlandi, S.; Dar, M. I.; Aghazada, S.; Jacopin, G.; Cavazzini, M.; Mosconi, E.; Gratia, P.; De Angelis, F.; Pozzi, G.; Graetzel, M.; Nazeeruddin, M. K. High Open-Circuit Voltage: Fabrication of Formamidinium Lead Bromide Perovskite Solar Cells Using Fluorene−Dithiophene Derivatives as Hole-Transporting Materials. *ACS Energy Letters* **2016**, *1*, 107−112.

(17) Kedem, N.; Brenner, T. M.; Kulbak, M.; Schaefer, N.; Levcenko, S.; Levine, I.; Abou-Ras, D.; Hodes, G.; Cahen, D. Light-induced increase of electron diffusion length in ap−n junction type $CH_3NH_3PbBr_3$ perovskite solar cell. *J. Phys. Chem. Lett.* **2015**, *6*, 2469−2476.

(18) Sheng, R.; Ho-Baillie, A.; Huang, S.; Chen, S.; Wen, X.; Hao, X.; Green, M. A. Methylammonium lead bromide perovskite-based solar cells by vapor-assisted deposition. *J. Phys. Chem. C* **2015**, *119*, 3545−3549.

(19) Talbert, E. M.; Zarick, H. F.; Orfield, N. J.; Li, W.; Erwin, W. R.; DeBra, Z. R.; Reid, K. R.; McDonald, C. P.; McBride, J. R.; Valentine, J.; Rosenthal, S. J.; Bardhan, R. Interplay of structural and compositional effects on carrier recombination in mixed-halide perovskite. *RSC Adv.* **2016**, *6*, 86947−86954.

(20) Edri, E.; Kirmayer, S.; Cahen, D.; Hodes, G. High open-circuit voltage solar cells based on organic−inorganic lead bromide perovskite. *J. Phys. Chem. Lett.* **2013**, *4*, 897−902.

(21) Heo, J. H.; Song, D. H.; Im, S. H. Planar CH3NH3PbBr3 Hybrid Solar Cells with 10.4% Power Conversion Efficiency, Fabricated by Controlled Crystallization in the Spin-Coating Process. *Adv. Mater.* **2014**, *26*, 8179−8183.

(22) Zarick, H. F.; Boulesbaa, A.; Puretzky, A. A.; Talbert, E. M.; DeBra, Z. R.; Soetan, N.; Geohegan, D. B.; Bardhan, R. Ultrafast carrier dynamics in bimetallic nanostructure-enhanced methylammonium lead bromide perovskites. *Nanoscale* **2017**, *9*, 1475−1483.

(23) Swainson, I. P.; Hammond, R. P.; Soullière, C.; Knop, O.; Massa, W. Phase transitions in the perovskite methylammonium lead bromide, $CH_3ND_3PbBr_3$. *J. Solid State Chem.* **2003**, *176*, 97−104.

(24) Mashiyama, H.; Kawamura, Y.; Kasano, H.; Asahi, T.; Noda, Y.; Kimura, H. Disordered Configuration of Methylammonium of $CH_3NH_3PbBr_3$ Determined by Single Crystal Neutron Diffractometry. *Ferroelectrics* **2007**, *348*, 182−186.

(25) Baikie, T.; Barrow, N. S.; Fang, Y.; Keenan, P. J.; Slater, P. R.; Piltz, R. O.; Gutmann, M.; Mhaisalkar, S. G.; White, T. J. A combined single crystal neutron/X-ray diffraction and solid-state nuclear magnetic resonance study of the hybrid perovskites $CH_3NH_3PbX_3$ (X= I, Br and Cl). *J. Mater. Chem. A* **2015**, *3*, 9298−9307.

(26) Fauth, F.; Boer, R.; Gil-Ortiz, F.; Popescu, C.; Vallcorba, O.; Peral, I.; Fulla, D.; Benach, J.; Juanhuix, J. The crystallography stations at the ALBA synchrotron, BL13-XALOC. *Eur. Phys. J. Plus* **2015**, *130*, 130−160.

(27) Rietveld, H. M. A profile refinement method for nuclear and magnetic structures. *J. Appl. Crystallogr.* **1969**, *2*, 65−71.

(28) Rodríguez-Carvajal, J. Recent advances in magnetic structure determination by neutron powder diffraction. *Phys. B* **1993**, *192*, 55−69.

(29) Kennedy, B. J.; Hunter, B. A.; Hester, J. R. Synchrotron x-ray diffraction reexamination of the sequence of high-temperature phases in $SrRuO_3$. *Phys. Rev. B: Condens. Matter Mater. Phys.* **2002**, *65*, 224103.

(30) Wignacourt, J. P.; Swinnea, J. S.; Steinfink, H.; Goodenough, J. B. Oxygen atom thermal vibration anisotropy in $Ba_{0.87}K_{0.13}BiO_3$. *Appl. Phys. Lett.* **1988**, *53*, 1753−1755.

(31) Onoda-Yamamuro, N.; Matsuo, T.; Suga, H. Calorimetric and IR spectroscopic studies of phase transitions in methylammonium trihalogenoplumbates (II). *J. Phys. Chem. Solids* **1990**, *51*, 1383−1395.

(32) Wang, G.; Li, D.; Cheng, H.-C.; Li, Y.; Chen, C.-Y.; Yin, A.; Zhao, Z.; Lin, Z.; Wu, H.; He, Q.; Ding, M.; Liu, Y.; Huang, Y.; Duan, X. Wafer-scale growth of large arrays of perovskite microplate crystals for functional electronics and optoelectronics. *Sci. Adv.* **2015**, *1*, e1500613.

(33) Liu, J.; Xue, Y.; Wang, Z.; Xu, Z.-Q.; Zheng, C.; Weber, B.; Song, J.; Wang, Y.; Lu, Y.; Zhang, Y.; Bao, Q. Two-dimensional $CH_3NH_3PbI_3$ perovskite: synthesis and optoelectronic application. *ACS Nano* **2016**, *10*, 3536−3542.

(34) Zhang, Y.; Du, J.; Wu, X.; Zhang, G.; Chu, Y.; Liu, D.; Zhao, Y.; Liang, Z.; Huang, J. Ultrasensitive Photodetectors Based on Island-Structured $CH_3NH_3PbI_3$ Thin Films. *ACS Appl. Mater. Interfaces* **2015**, *7*, 21634−21638.

(35) Lu, H.; Tian, W.; Cao, F.; Ma, Y.; Gu, B.; Li, L. A Self-Powered and Stable All-Perovskite Photodetector−Solar Cell Nanosystem. *Adv. Funct. Mater.* **2016**, *26*, 1296−1302.

(36) Deng, H.; Dong, D.; Qiao, K.; Bu, L.; Li, B.; Yang, D.; Wang, H.-E.; Cheng, Y.; Zhao, Z.; Tang, J.; Song, H. Growth, patterning and alignment of organolead iodide perovskite nanowires for optoelectronic devices. *Nanoscale* **2015**, *7*, 4163−4170.

(37) Zhuo, S.; Zhang, J.; Shi, Y.; Huang, Y.; Zhang, B. Self-Template-Directed Synthesis of Porous Perovskite Nanowires at Room Temperature for High-Performance Visible-Light Photodetectors. *Angew. Chem., Int. Ed.* **2015**, *54*, 5693−5696.

(38) Deng, H.; Yang, X.; Dong, D.; Li, B.; Yang, D.; Yuan, S.; Qiao, K.; Cheng, Y.-B.; Tang, J.; Song, H. Flexible and semitransparent organolead triiodide perovskite network photodetector arrays with high stability. *Nano Lett.* **2015**, *15*, 7963−7969.

(39) Li, D.; Dong, G.; Li, W.; Wang, L. High performance organic-inorganic perovskite-optocoupler based on low-voltage and fast response perovskite compound photodetector. *Sci. Rep.* **2015**, *5*, 7902.

(40) Dong, R.; Fang, Y.; Chae, J.; Dai, J.; Xiao, Z.; Dong, Q.; Yuan, Y.; Centrone, A.; Zeng, X. C.; Huang, J. High-Gain and Low-Driving-Voltage Photodetectors Based on Organolead Triiodide Perovskites. *Adv. Mater.* **2015**, *27*, 1912−1918.